
Study of Direct-Drive, DT-Gas-Filled-Plastic-Capsule Implosions Using Nuclear Diagnostics on OMEGA

Introduction

High-gain inertial confinement fusion (ICF) requires uniform compression of a spherical capsule to a state of high density and temperature;^{1–3} current research is aimed at finding ways to achieve this goal. This article describes how a range of traditional and new nuclear diagnostics are used to study the compression performance of deuterium-tritium (DT)-filled target capsules imploded by direct laser drive on LLE’s 60-beam OMEGA laser system.⁴ The sensitivity of the implosion performance to the uniformity of laser power deposition is studied by measuring the fuel and shell areal densities (ρR) and the shell electron temperature (T_e). These parameters are studied using the first comprehensive set of separate spectral measurements of deuterons, tritons, and protons (“knock-ons”) elastically scattered from the fuel and shell by 14.1-MeV DT fusion neutrons.

To achieve fusion ignition, a DT-filled target needs sufficient compression to form two different regions: a small mass with low density but high temperature in the center (the “hot spot,” with $T_i \sim 10$ keV) and a large mass of high-density, low-temperature fuel surrounding this hot spot. The 3.5-MeV DT alphas generated in the central hot spot (with $\rho R \sim 0.3$ g/cm²) are stopped in the fuel, thereby propagating a thermonuclear burn. Two approaches to achieving this objective are indirect- and direct-drive implosions. For the indirect-drive approach, where laser beams irradiate the inner wall of a high-Z radiation case (hohlraum), laser energy is first converted to soft x rays, which subsequently compress the capsule. For the direct-drive approach, the laser beams directly irradiate and compress the target. The National Ignition Facility (NIF), which has both indirect- and direct-drive capabilities and is under construction at Lawrence Livermore National Laboratory, is designed to achieve this ignition objective. Experiments on OMEGA are currently investigating many aspects of the implosion physics relevant to future NIF experiments with scaled experimental conditions. For example, the OMEGA cryogenic program will study energy-scaled implosions based on NIF ignition target designs.⁵

OMEGA is a Nd-doped glass laser facility that can deliver 60 beams of frequency-tripled UV light (351 nm) with up to 30 kJ in 1 to 3 ns with a variety of pulse shapes; both direct and indirect drive are possible.⁴ Early direct-drive experiments on OMEGA have achieved high temperatures ($T_i \sim 15$ keV) and high fusion yields (for example, DT neutron yield $\sim 10^{14}$ and DD neutron yield $\sim 10^{12}$).⁶ In particular, a series of implosions of room-temperature capsules with gas fill (0 to 30 atm of either D₂ or D³He) and plastic shells (CH, 10 to 35 μ m thick) have recently been conducted with a variety of laser pulse shapes, irradiation uniformities, etc.^{7–11} These implosions generate typical fuel areal densities (ρR_{fuel}) of ~ 5 to 15 mg/cm² and shell areal densities (ρR_{shell}) > 50 mg/cm². Part of their importance lies in their relevance to OMEGA cryogenic-target implosions and the insights they provide into implosion physics of direct-drive ICF.

The OMEGA experiments included in this article involved room-temperature capsules with DT-gas fill and CH shells. The nominal parameters were 20- μ m shell thickness and 15-atm fill pressure. These types of capsules have total masses similar to those of OMEGA cryogenic targets and are expected to have comparable stability properties under similar experimental conditions.^{5,7} An OMEGA cryogenic capsule consists of three parts: a central part with low-pressure (triple-point vapor pressure) D₂ or DT gas (0.2 atm at ~ 19 K), a main fuel layer (~ 90 μ m of D₂ or DT ice), and a 1- to 3- μ m CH overcoat. The CH shell of a room-temperature target simulates the fuel part (DT ice) of a cryogenic target, and the fill gas simulates the hot-spot-forming central DT gas in a cryogenic target.⁵ The hydrodynamics are expected to differ in detail, in part due to the difference in the equation of state, ablation rate, and implosion velocity. Nevertheless, many aspects of high-energy-density physics and the target performances of cryogenic targets can be studied with these surrogate targets under current experimental conditions, including the effects of irradiation uniformity. The experiments also provide useful data for the development of advanced diagnostics (such as high-resolution, charged-particle spectroscopy¹²) and for benchmarking computer simulations.¹³

A primary emphasis in this study was the dependence of capsule performance on laser irradiation uniformity; the next section provides motivation by describing the importance of irradiation uniformity to the physics of capsule implosion performance. Subsequent sections (1) describe the experiments under study here, utilizing DT-filled capsules with CH shells and different laser-smoothing techniques; (2) discuss the measurement of knock-on spectra and the relationships between these measurements and the characteristics of imploded capsules; and (3) discuss the performance of imploded core and shell under different conditions, showing that 15-atm-DT capsules with appropriate laser smoothing achieved a moderate convergence ratio ($Cr \sim 12$ to 15); ρR_{fuel} and ρR_{shell} were determined to be ~ 15 mg/cm² and ~ 60 mg/cm², respectively.

Laser Drive Characteristics and Capsule Performance

Successful direct-drive implosions require control of Rayleigh–Taylor (RT) instability because direct-drive targets are susceptible to this instability during both acceleration and deceleration phases.^{5,7} This control requires shell integrity throughout the whole acceleration phase, which can be accomplished by a spherical target being irradiated uniformly. The instability is seeded by laser illumination nonuniformity and also by target imperfections (roughness on the outer ablative surface and/or the inner fuel–shell interface).⁷ During the acceleration phase, this instability can occur at the ablation surface and propagate to the fuel–shell interface, adding roughness to the inner shell surface and also feeding back out to the ablation surface; in the worst case, this could lead to shell breakup. During the deceleration phase, the distortions at the fuel–shell interface grow and result in the mixing of fuel and shell materials, which degrades target performance.

For the shots studied here, two approaches were used to control instabilities and improve target performance. The first was the choice of laser pulse shape. A high-shock-strength (high adiabat), 1-ns square laser pulse was used to maximize the ablation rate and reduce RT growth. Though a gradually rising pulse (low adiabat) produces, in principle, a larger target compression than a sharply rising pulse, because of lower fuel and shell isentropes,^{1,2} a low-shock-strength pulse generates a lower ablation rate and smaller in-flight shell thickness, leading to more instability for direct-drive implosions. This has been demonstrated in earlier experiments, where better target performance was obtained with a 1-ns square pulse than with other pulse types for room-temperature targets.^{8,9} Simulations have predicted that another advantage to using the 1-ns square pulse to implode room-temperature capsules with 20- μm -CH shells is that the target hydrodynamic and stability properties

are similar to those that result from using a shaped pulse with cryogenic targets (for example, the OMEGA $\alpha = 3$ design⁷).

The second approach is improved laser-irradiation uniformity. In discussing deviations from illumination uniformity, we distinguish two sources: Beam-to-beam energy imbalance causes low-order mode perturbations (mode number $\ell < 10$), while nonuniformities within individual beams generate higher-order perturbations ($\ell > 10$). To achieve a level of 1% or less for on-target irradiation nonuniformity, different beam energies must be matched to within an rms deviation of 5%.^{5,7} In the series of implosions studied here, an energy balance within 3% to 25% rms was achieved; however, after taking into account the effect of the laser-beam overlap on the target surface (as shown in Fig. 86.11), low-mode rms uniformity was between 1% and 9%, with an average $\leq 5\%$.

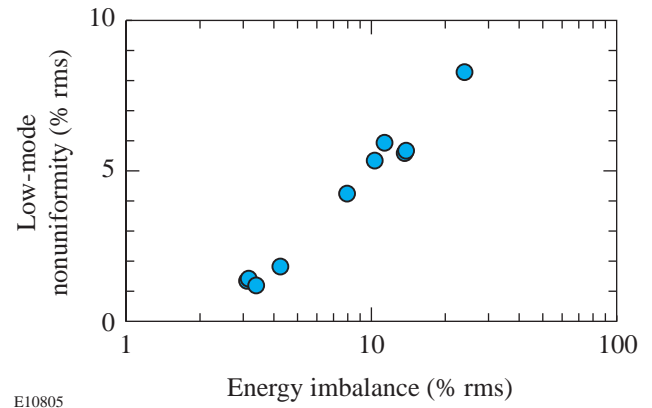


Figure 86.11

The low-mode rms irradiation nonuniformity plotted as a function of the beam energy imbalance. In general, a better energy balance results in better low-mode rms irradiation uniformity.

Single-beam uniformity is improved by two-dimensional smoothing by spectral dispersion (2-D SSD) combined with other smoothing techniques such as distributed phase plates (DPP's) and distributed polarization smoothing (PS).⁷ The two smoothing conditions used in this study were 0.35-THz-bandwidth, 3-color-cycle 2-D SSD and 1.0-THz-bandwidth, single-color-cycle 2-D SSD with PS. Theoretical simulations and recent experiments have demonstrated that PS improves irradiation uniformity by a factor of $\sim \sqrt{2}$ for higher-order perturbations ($\ell > 10$). The combination of PS with high-bandwidth 2-D SSD is expected to result in on-target nonuniformity $< 1\%$ after 300 ps.^{5,7,14}

Experiments

The OMEGA experiments reported here used 60 beams of frequency-tripled (351-nm) UV light to directly drive the targets. Targets were room-temperature capsules with DT gas enclosed in a CH shell. The actual DT-gas pressure was in the range of 11 to 15 atm. The CH-shell thickness was 19 to 20 μm , and the capsule diameters were 920 to 960 μm . Laser energy ranged from 20 to 23 kJ, with a typical intensity of $\sim 1 \times 10^{15}$ W/cm², and the laser-beam spot size on target was ~ 1 mm. The laser pulse was approximately square with a 1-ns duration, with rise and decay times of ~ 150 ps. Good pulse-shape repeatability was obtained, and the beam-to-beam laser energy balance was typically $\sim 5\%$ rms. Two laser configurations were used. In the first, individual beams were smoothed using 3-color-cycle 2-D SSD along two axes with a bandwidth of 0.35 THz. In the second, beams were smoothed by single-color-cycle 2-D SSD, with a 1.0-THz bandwidth, and PS using a birefringent wedge.

The primary DT neutron yields were measured using Cu activation.¹⁵ For this series of experiments, primary DT neutron yields of 10^{12} to 10^{13} were obtained, with an estimated measurement error of $\sim 10\%$. Ion temperatures T_i were measured using neutron time-of-flight (NTOF) Doppler widths.^{16–18} Typical values were 3.5 to 5 keV, with a measurement error of ~ 0.5 keV. Fusion burn history was obtained with the neutron temporal detector (NTD),¹⁹ and the typical fusion burn durations here were 140 to 190 ps with bang times occurring at several hundred picoseconds after the end of the laser pulse.

To obtain the areal densities for compressed fuel and shell (a fundamental measure of the implosion dynamics and quality), and to address other issues (such as the measurement of shell T_e , electrostatic potential due to capsule charging, etc.), spectra of emerging charged particles were measured with two magnet-based charged-particle spectrometers (CPS-1 and CPS-2)^{20,21} and several “wedge-range-filter (WRF)” spectrometers.^{11,22} The charged particles [knock-on deuterons (KOD), tritons (KOT), and protons (KOP)] are elastically scattered from the fuel and shell by 14.1-MeV DT neutrons.^{23,24} This is currently the only technique for studying the fuel and shell areal densities of DT capsule implosions on OMEGA. Other possible methods include neutron activation²⁵ and measurement of secondary^{26,27} and tertiary products (neutrons and protons^{27–29}), but these methods are currently impractical because of certain technical limitations.

CPS-1 and CPS-2 are nearly identical, and each uses a 7.6-kG permanent magnet^{20,21} constructed of a neodymium-iron-boron alloy with a steel yoke. Incoming particles are collimated by a slit whose width can be varied between 1 and 10 mm (giving an acceptance of 10^{-6} to 10^{-5} of the total yield), as appropriate for expected flux levels. The magnet separates particles into different trajectories according to the ratio of momentum to charge. Pieces of CR-39, used as particle detectors, are positioned throughout the dispersed beam normal to the particle flux. Both the energy and the species of the particle generating a track in CR-39 can be determined through the combined knowledge of its trajectory (determined by its position on the CR-39) and the track diameter. Particles with the same gyro radius, such as 8-MeV tritons and 12-MeV deuterons, are easily distinguished since their very different stopping powers generate measurably different track sizes in the CR-39 (the larger the stopping power, the larger the track). This configuration allows coverage over the proton energy range from 0.1 MeV to 40 MeV. The energy calibration uncertainty varies with particle energy, being about 30 keV at 2 MeV and about 100 keV at 15 MeV. The two spectrometers are 101° apart, thereby enabling studies of implosion symmetry. CPS-2 (CPS-1) is placed inside (outside) the 165-cm-radius OMEGA chamber at 100 cm (235 cm) from the target.

The WRF spectrometers, which are described in detail elsewhere,^{11,22} provide proton spectra by analyzing the distributions of proton-track diameters in a piece of CR-39 that is covered during exposure by an aluminum ranging filter with continuously varying thickness. The current energy calibration is accurate to about 0.15 MeV at 15 MeV. These spectrometers are simple and compact, allowing them to be used at multiple positions during a shot for symmetry studies and placed close to the target for good statistics when proton yields are low (down to about 5×10^5).

To analyze the measurements made during these experiments, the implosions were modeled with the one-dimensional hydrodynamic calculation code *LILAC*.³⁰ Several important physical models were used in the calculation, such as the tabulated equation of state (*SESAME*), flux-limited electron transport (with a flux limiter of $f=0.06$), local thermodynamic equilibrium (LTE), opacities for multigroup radiation transport, and inverse-bremsstrahlung-absorption energy deposition through a ray-trace algorithm in the underdense plasma. No effect of fuel-shell mix was included.

Knock-on Particles and Their Spectra

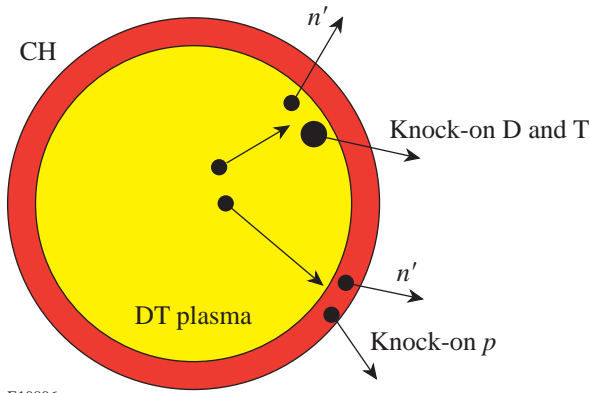
Knock-on particles are generated in a two-step process. A 14.1-MeV neutron is first generated from a DT fusion reaction. These neutrons usually escape the capsule without interacting. A small fraction of them (of the order of $\sim 0.1\%$), however, elastically scatter off either fuel D or T or CH-shell p , as described in Eqs. (1)–(4) and depicted schematically in Fig. 86.12. Information about the compressed fuel is carried out by these knock-on D and T; information about the compressed shell is carried out by knock-on p and is also contained in the energy downshifts of knock-on D and T spectra:

$$D + T \rightarrow \alpha(3.5 \text{ MeV}) + n(14.1 \text{ MeV}), \quad (1)$$

$$n(14.1 \text{ MeV}) + T \rightarrow n' + T(\leq 10.6 \text{ MeV}), \quad (2)$$

$$n(14.1 \text{ MeV}) + D \rightarrow n' + D(\leq 12.5 \text{ MeV}), \quad (3)$$

$$n(14.1 \text{ MeV}) + p \rightarrow n' + p(\leq 14.1 \text{ MeV}). \quad (4)$$



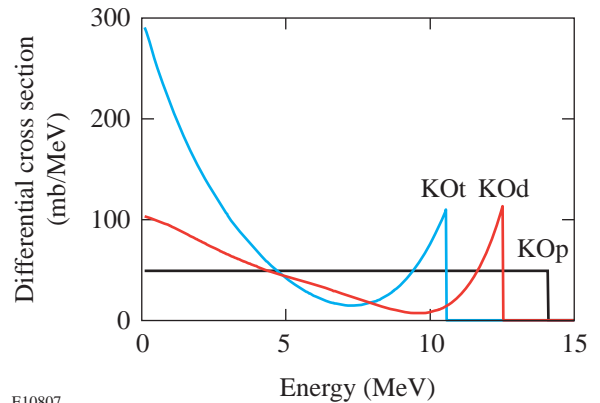
E10806

Figure 86.12

A schematic illustration of the knock-on processes in an imploded capsule. The central fuel part typically has an initial radius of 450 to 475 μm and a DT-gas fill of 15 atm. The initial shell layer is constructed of CH with a thickness of 19.5 to 20 μm . Primary 14.1-MeV DT neutrons, generated in the fuel, elastically scatter deuterons (KOd) and tritons (KOt) out of the fuel and protons (KOp) out of the shell. Consequently, information from the compressed core is carried out by these knock-on deuterons and tritons, and information from the compressed shell is carried out by knock-on protons. The energy downshifts of knock-on D and T spectra also contain information about the shell.

Figure 86.13 illustrates the differential cross sections of knock-on processes. When the collisions are head-on, the characteristic end-point energy for T (D) [p] is 10.6 MeV (12.5 MeV) [14.1 MeV]. The well-defined, high-energy peak for a knock-on deuteron (triton) spectrum represents about 15.7% (13.5%) of the total cross section and corresponds to an energy region of 9.6 to 12.5 MeV (7.3 to 10.6 MeV). For a model-independent determination of ρR_{fuel} , the knock-on diagnostic usually uses only these high-energy peaks. For knock-on protons, the cross section is virtually flat from 0 to 14.1 MeV because the neutron and proton masses are nearly identical. Because of a possible time-dependent distortion occurring in the low-energy region, however, only the flat region is used here. Two important parameters for this diagnostic are the number of knock-on particles and the downshifts of the knock-on spectra. The knock-on numbers provide information about the ρR of the layer (core or shell) in which they are produced, and the energy loss of these particles provides additional information about the ρR traversed.

It has been shown that, for a hot-spot model of the compressed fuel (where all primary neutrons are produced in an infinitesimal, high-temperature region at the center of a uniform-density DT plasma), ρR_{fuel} is related to the knock-on



E10807

Figure 86.13

Differential cross sections for elastic scattering of 14.1-MeV neutrons on deuterons, tritons, and protons, where the energy is the scattered ion energy. When these collisions are head-on, the characteristic end-point (maximum) energy for T (D) [p] is 10.6 MeV (12.5 MeV) [14.1 MeV]. The high-energy peak for knock-on deuterons (tritons) contains about 15.7% (13.5%) of the total cross section, which corresponds to an energy region of 9.6 to 12.5 MeV (7.3 to 10.6 MeV). [For deuterons and tritons, the integral under the high-energy peak gives an effective cross section that is used in Eq. (5)]. For knock-on protons, the cross section is flat from 0 to 14.1 MeV, and an integral over a 1-MeV interval gives an effective cross section that is used in Fig. 86.14.

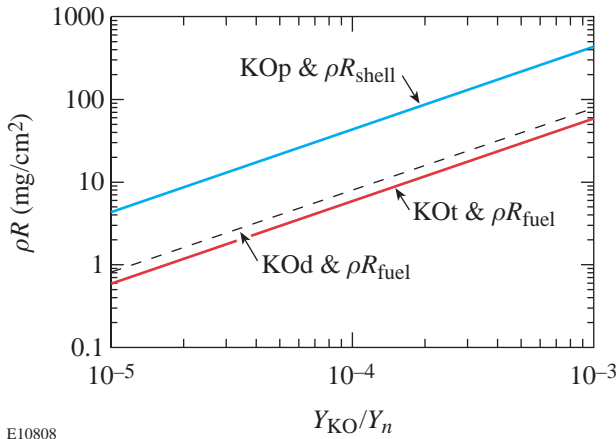
yield by the equation^{23,24}

$$\rho R_{\text{fuel}} = \frac{(2\gamma + 3)m_p}{(\gamma\sigma_d^{\text{eff}} + \sigma_t^{\text{eff}})} \frac{Y_{\text{KOd}} + Y_{\text{KOt}}}{Y_n}, \quad (5)$$

where Y_n is the measured primary neutron yield, Y_{KOd} and Y_{KOt} are deuteron and triton knock-on yields under the high-energy peak of their spectra (see Fig. 86.13); σ_t^{eff} (σ_d^{eff}) is the effective cross-section of knock-on triton (deuteron) as defined in Fig. 86.13; m_p is the proton mass; and $\gamma = n_d/n_t$. Similarly, the yield of knock-on protons, which are exclusively generated in the CH shell, can be shown to be related to ρR_{shell} by the equation

$$\rho R_{\text{shell}} = \frac{(\gamma + 12)m_p}{\gamma\sigma_p^{\text{eff}}} \frac{Y_{\text{KO}p}}{Y_n}, \quad (6)$$

where $Y_{\text{KO}p}$ is the measured knock-on- p yield in a 1-MeV range (see Fig. 86.13); σ_p^{eff} is an effective cross section for knock-on protons; and $\gamma = n_H/n_C$ (where n_H and n_C are the number densities of the hydrogen and carbon atoms, respectively, in the shell). Under some circumstances, it is useful to modify Eq. (5) for use with the “uniform” model, in which primary neutrons are generated throughout the volume containing deuterons and tritons, by multiplying the right-hand side by a factor of 1.33. Figure 86.14 displays inferred values



E10808

Figure 86.14

Areal density versus the ratio of knock-on particle yield to primary neutron yield. For knock-on D and T, a hot-spot model is assumed and the yields under the high-energy peaks are used (as described in Fig. 86.13’s caption). For knock-on p , a hot-spot model is assumed and the yield per MeV in the flat region is used.

of ρR as a function of the measured ratios of knock-on yield to primary neutron yield. The model-independent use of Eq. (5) breaks down when the total areal density exceeds about 100 mg/cm² because the knock-on spectra become sufficiently distorted by slowing-down effects that measurements can become ambiguous; the accurate determination of ρR_{fuel} will then have to rely on the guidance of model-dependent simulations.

The potential importance of knock-on particle measurements was realized some years ago, and measurements with both limited spectral resolution and a small number of knock-on particles (around 30) were subsequently obtained.^{23,24} Those measurements relied on range-filter data in the form of “coincident” (front-side and back-side) tracks generated in a CR-39 nuclear track detector or in nuclear emulsions. This early work relied on detailed assumptions about the spectra of knock-on particles, which were estimated in indirect ways from other diagnostic data (for example, from the downshifted D³He protons).²³ In contrast, charged-particle spectroscopy, as described here, measures the whole spectrum directly for each particle. With hundreds to thousands of knock-on particles being simultaneously detected from an individual implosion, comprehensive and high-resolution knock-on spectra are readily obtained.

Figure 86.15 shows sample spectra obtained by CPS-2 for shot 20231. For this shot, the capsule was filled with 12.3 atm of DT gas and had a 19.1- μm -thick CH shell. The laser energy was 22.1 kJ, and the primary neutron yield was $7.1(\pm 0.7) \times 10^{12}$. The bandwidth of the 2-D SSD was 0.35 THz, and no polarization smoothing (PS) was applied. The beam-to-beam energy balance was 13.7% rms, and the on-target, low-mode rms uniformity was 5.6% because of beam overlap on the target surface. An ion temperature of $T_i \cong 4.0(\pm 0.5)$ keV was obtained. The fusion burn occurred at $1810(\pm 50)$ ps and lasted for $180(\pm 25)$ ps. Figure 86.15(a) provides the knock-on T spectrum with a yield of about 5.7×10^8 tritons under the high-energy peak (between 3 to 10 MeV). The whole spectrum is downshifted by ~ 4 MeV (as described in the figure caption). Figure 86.15(b) shows the knock-on D spectrum with a yield of about 4.8×10^8 deuterons under the high-energy peak (between 3.5 to 12 MeV). An energy loss of about ~ 3 MeV, relative to the birth spectrum, is measured. Figure 86.15(c) displays the knock-on p spectrum, with a yield of about $5.7 \times 10^8/\text{MeV}$ protons in the flat region between 8 to 12 MeV. The end point of this spectrum is about 14 MeV because protons scattered from the outer part of the shell lose no energy. We note that CPS yield measurements represent an integral over

the fusion burn duration, so an inferred ρR value represents an average over the burn. In addition, the fact that the source of neutrons is distributed over a finite volume of fuel means that inferred ρR values represent spatial averages.

The measured knock-on spectra for shot 20698 are shown in Fig. 86.16. The capsule was filled with 15 atm of DT gas and had a 20- μm CH shell. The laser energy was 23.8 kJ, and the primary neutron yield was $1.4(\pm 0.1) \times 10^{13}$. In contrast to shot 20231, polarization smoothing was applied for this shot and the 2-D SSD bandwidth was increased to 1.0 THz. The beam-

to-beam energy balance (3.1% rms) and the on-target low-mode rms uniformity (1.3% rms) were thus improved. An ion temperature of $T_i \cong 4.1(\pm 0.5)$ keV was obtained. The fusion burn occurred at $1750(\pm 50)$ ps and lasted for $170(\pm 25)$ ps. Figure 86.16(a) shows the knock-on T spectrum, with a yield of about 1.2×10^9 tritons under the high-energy peak (between 2.5 to 10 MeV). The whole spectrum is downshifted by 4.8 MeV. Figure 86.16(b) shows the knock-on D spectrum, with a yield of about 1.7×10^9 deuterons under the high-energy peak (between 3.5 to 12 MeV). An energy loss of about 4.1 MeV is measured. Figure 86.16(c) shows the knock-on p

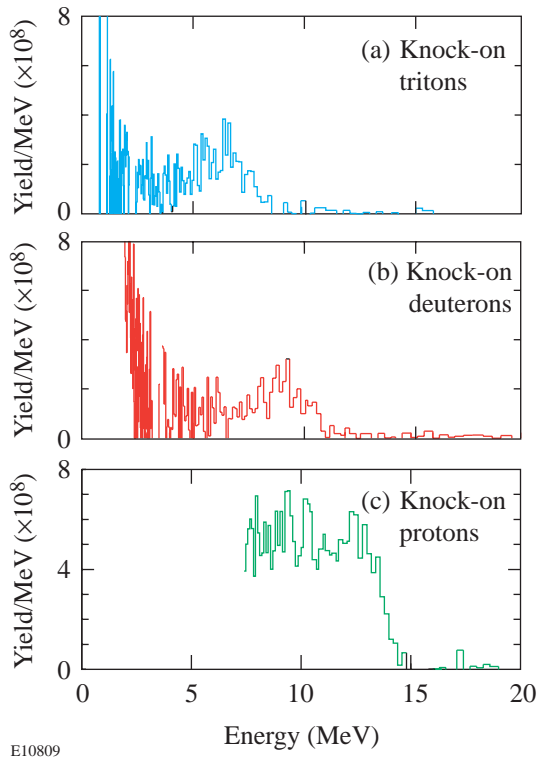


Figure 86.15
Knock-on spectra measured by CPS-2 for shot 20231. The capsule was filled with 12.3 atm of DT gas and had a 19.1- μm -thick CH shell. The laser energy was 22.1 kJ, and the primary neutron yield was 7.1×10^{12} . The bandwidth of 2-D SSD was 0.35 THz, and no PS was applied. (a) The knock-on T spectrum with a yield of about 5.7×10^8 tritons under the high-energy peak (between 3 to 10 MeV). The whole spectrum is downshifted by ~ 4 MeV (determined by the energy at which the yield/MeV reaches half of its peak value on the high-energy end of the spectrum). (b) The knock-on D spectrum with a yield of about 4.8×10^8 deuterons under the high-energy peak (between 3.5 to 12 MeV). An energy loss of about ~ 3 MeV is measured. (c) The knock-on p spectrum with a yield/MeV of about $5.7 \times 10^8/\text{MeV}$ protons in the flat region between 8 to 12 MeV. The end point of this spectrum is about 14 MeV, reflecting the fact that particles scattered from the outer part of the shell have no energy loss.

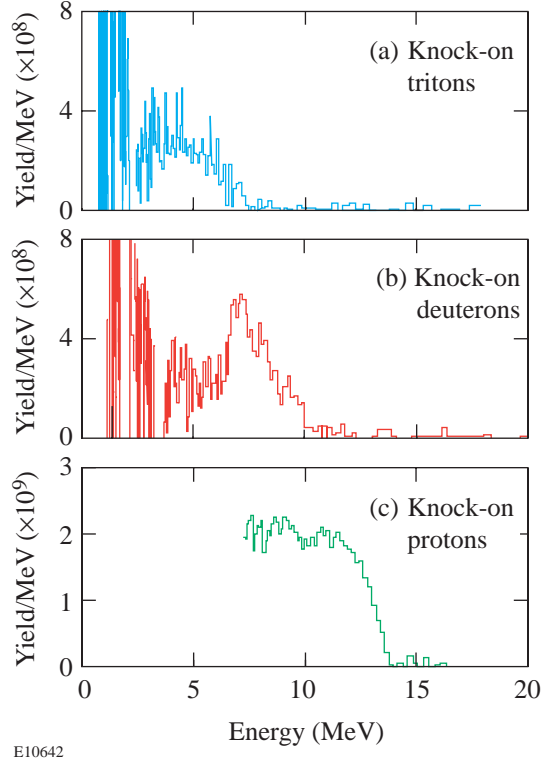


Figure 86.16
Knock-on spectra for shot 20698, measured by CPS-2. The capsule is filled with 15 atm of DT gas and has a 20- μm CH shell. For this shot, the laser energy was 23.8 kJ, and the primary neutron yield was 1.4×10^{13} . The 2-D SSD bandwidth was 1.0 THz, and polarization smoothing was applied. (a) The knock-on T spectrum, with a yield of about 1.2×10^9 tritons under the high-energy peak (between 2.5 to 10 MeV). The whole spectrum is downshifted by 4.8 MeV. (b) The knock-on D spectrum, with a yield of about 1.7×10^9 deuterons under the high-energy peak (between 3.5 to 12 MeV). An energy loss of about 4.1 MeV is measured. (c) The knock-on p spectrum, with a yield of about $2.0 \times 10^9/\text{MeV}$ protons in the flat region between 8 to 12 MeV. As in Fig. 86.15, the end point of this spectrum is about 14 MeV, reflecting the fact that particles scattered from the outer part of the shell have no energy loss.

spectrum, with a yield of about 2.0×10^9 /MeV in the flat region between 8 to 12 MeV. The end point of this spectrum is about 14 MeV, as for shot 20231. Relative to shot 20231, the primary neutron yield in shot 20698 is higher by a factor of ≈ 1.95 , and the knock-on particle yields are higher by factors of ≈ 3.48 (deuteron) and ≈ 3.45 (proton). In addition, because of increased compression, the energy loss of the knock-on particles from the fuel is greater by 15% to 30%.

Results and Discussions

1. Core Performance of Moderate-Convergence Capsule Implosions

In this section we examine the effects of illumination uniformity on core performance for moderate-convergence capsule implosions, as characterized by measurements of primary neutrons and knock-on charged particles. We start with the primary neutron yield, which provides one direct overall measure of core performance because of its strong dependence on ion temperature and density. Next we look at the yields of knock-on deuterons (Y_{KOd}) and tritons (Y_{KOt}), which provide a measure of ρR_{fuel} , and thus the amount of compression (which is quantified by the convergence ratio Cr, defined as a ratio of the initial fuel radius to the final compressed fuel radius). After showing that the data demonstrate an improvement in performance with improved laser smoothing, we examine comparisons of the data with numerical simulations. These comparisons suggest that the poorer performance observed with less smoothing is due to intrinsically 2-D or 3-D effects such as instabilities and mix.

Primary neutron yields between 3×10^{12} and 1.4×10^{13} were obtained, and, in general, better energy balance resulted in higher primary neutron yield. The highest yield was obtained for the shot with a low-mode rms nonuniformity of $\sim 1.3\%$ (energy balance to within 3.1%). Once on-target, low-mode nonuniformity due to beam imbalance has been decreased to the 5% rms range, single-beam nonuniformity becomes more important for capsule performance through its effects on high-order-mode perturbations. This is illustrated in Fig. 86.17(a), which indicates that beam smoothing with 1-THz, 2-D SSD + PS results in a primary yield ($Y_n \sim 1.1 \times 10^{13}$) about 80% higher than that obtained with 0.35-THz, 2-D SSD and no PS ($Y_n \sim 6.2 \times 10^{12}$). Since the ion temperature is found to be relatively insensitive to rms uniformity improvement, as shown in Fig. 86.17(b), higher Y_n must result from a higher ion density due to improved fuel compression.

While determining the ρR_{fuel} from knock-on yields, efforts to match the experimental primary yields by assuming differ-

ent temperature profiles led to a preference of the uniform model over the hot-spot model because highly peaked temperature profiles led to yields that were too low, so the ρR_{fuel} versus yield relationships shown in Fig. 86.14 must be modified. The corresponding inferred convergence ratio is

$$\text{Cr} = \sqrt{\rho R_{\text{fuel}} / \rho R_{\text{fuel}0}},$$

where $\rho R_{\text{fuel}0}$ is the fuel ρR before compression. As shown in Fig. 86.18, the data led to average values of $\rho R_{\text{fuel}} \sim 9.3 \text{ mg/cm}^2$ (Cr ~ 12) for the shots using 0.35-THz, 2-D SSD and $\rho R_{\text{fuel}} \sim 15 \text{ mg/cm}^2$ (Cr ~ 15) for 1-THz, 2-D SSD + PS. Increasing the smoothing rate increased ρR_{fuel} by $\sim 60\%$ and Cr by $\sim 25\%$.

One-dimensional (1-D) simulations were carried out for the studied shots. Figure 86.19 shows an example of how a measured knock-on deuteron spectrum compares with a prediction for shot 20698. Relative to the data, the simulation has a similar spectral shape, a similar energy downshift, and a similar, if somewhat higher, yield. Figures 86.20 to 86.23 provide an overview of data-to-simulation comparisons. Since the effects of beam smoothing are intrinsically 2-D or 3-D, the 1-D code predicts no difference due to smoothing; this can be seen in Figs. 86.20 and 86.21, which show that nearly all the shots are predicted to have the same values of ρR_{fuel} , Cr, and T_i , with small differences due only to the small differences in capsule parameters and total laser energy. On the other hand,

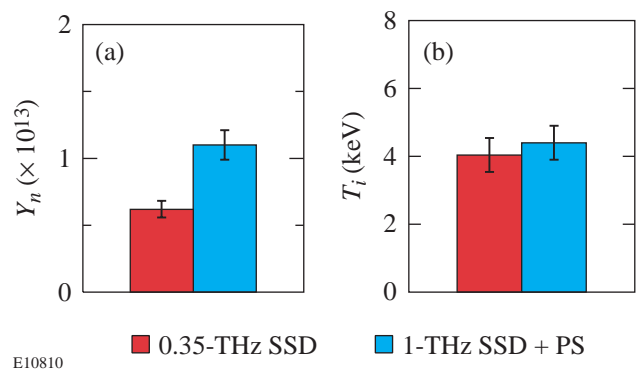


Figure 86.17

(a) Average primary yields achieved for two different single-beam smoothing conditions. The yield increases by about 80% when uniformity is improved using 1-THz, 2-D SSD + PS. (b) The yield-averaged ion temperature is insensitive to the improvement in uniformity. Consequently, the significant increase of primary yields cannot be attributed to the ion temperatures and is instead probably a consequence of an increase in ion density due to better fuel compression. The error bars display statistical uncertainties.

the measured values of ρR_{fuel} (or Cr) improve significantly for increased laser smoothing and approach the predicted values with 1-THz, 2-D SSD + PS. Other parameters also increase when smoothing is improved, including Y_n and Y_{KOd} , whose ratios to predicted values (YOC and $Y_{\text{KOd}}/Y_{1\text{-D}}$, respectively) are shown in Fig. 86.22. Plotting the ratio of measured to predicted values of Y_{KOd}/Y_n against measured Cr, in Fig. 86.23, shows that it approaches unity for full beam smoothing. This suggests that the improvement of single-beam irradiation uniformity results in increased compression through the reduction of 2-D phenomena such as instabilities and mix.

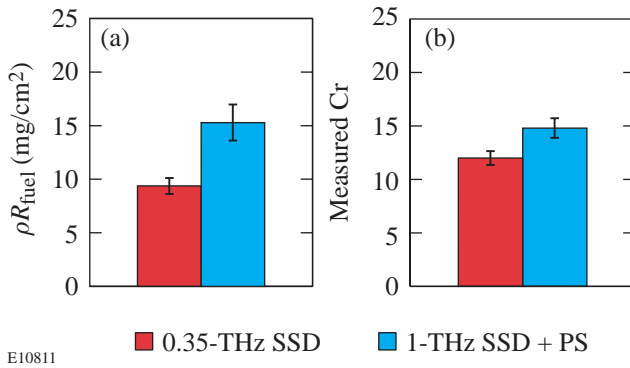


Figure 86.18 (a) Average fuel areal densities measured in experiments using 0.35-THz, 2-D SSD ($\rho R_{\text{fuel}} \sim 9.3 \text{ mg}/\text{cm}^2$) and 1-THz, 2-D SSD + PS ($\rho R_{\text{fuel}} \sim 15 \text{ mg}/\text{cm}^2$). A significant increase of the ρR_{fuel} ($\sim 60\%$) is obtained using 1.0-THz, 2-D SSD + PS. (b) Experimentally measured convergence ratios. Cr ~ 12 for shots using 0.35-THz, 2-D SSD, and Cr ~ 15 for shots using 1-THz, 2-D SSD + PS. The error bars display statistical uncertainties.

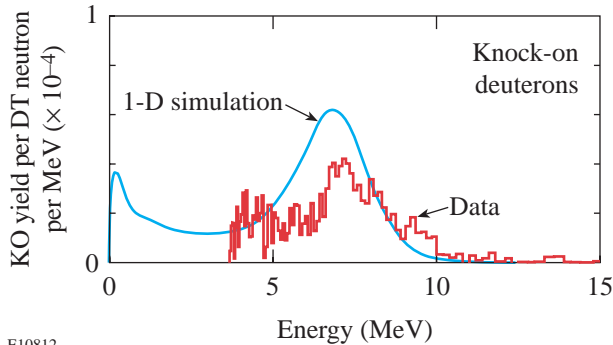


Figure 86.19 A comparison of the experimentally measured knock-on deuteron spectrum and the 1-D LILAC-predicted spectrum for shot 20698.

The credibility of this hypothesis is increased by more elaborate simulations that incorporate effects of Rayleigh–Taylor, Richtmyer–Meshkov, and Bell–Plesset instabilities, and 3-D Haan saturation^{5,7} in the postprocessing of 1-D calculation results. It was shown that using 0.35-THz, 2-D SSD without PS can result in a mix width that exceeds the in-flight shell thickness.^{5,7} The shell integrity is thus reduced, and the capsule compression is degraded. In contrast, the calculations show that with full beam smoothing (on-target beam nonuniformity less than 1% after 300 ps), the mix width is significantly smaller than the in-flight shell thickness.

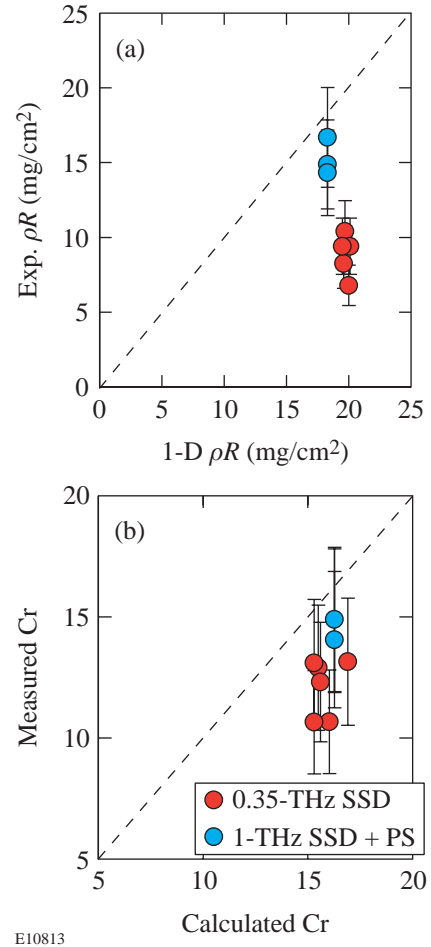
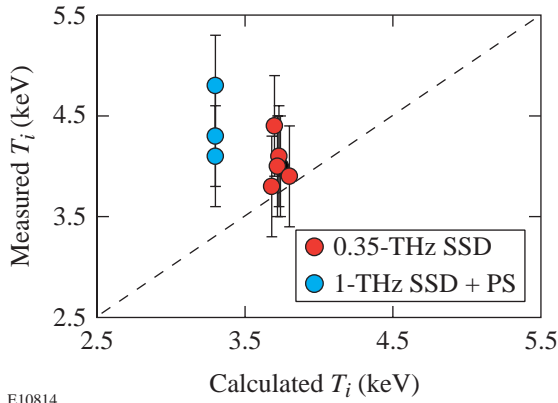
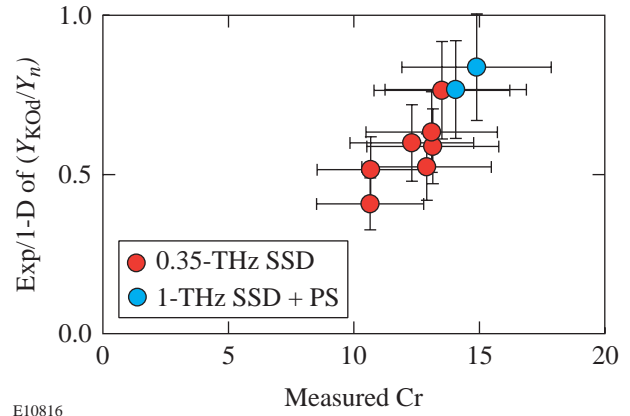


Figure 86.20 (a) Measured ρR_{fuel} versus 1-D simulation prediction. For the shots with 0.35-THz, 2-D SSD, the average measured ρR_{fuel} is about 60% of the prediction. For the shots with 1-THz, 2-D SSD + PS, an average of $\sim 80\%$ of the predicted ρR_{fuel} is measured. This comparison suggests that the improvement in irradiation uniformity makes implosions more 1-D-like. (b) The measured convergence ratio plotted against the calculation. The experimental data are slightly but consistently lower than those of 1-D predictions. The error bars display experimental uncertainties ($\sim 10\%$ for neutrons, $\sim 20\%$ for charged particles).



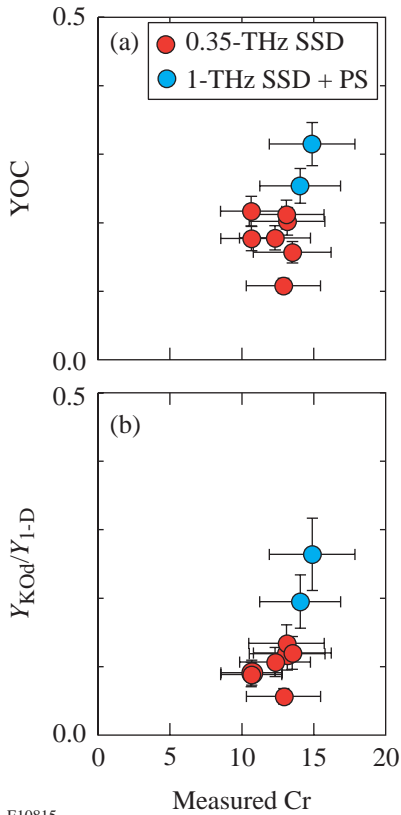
E10814

Figure 86.21
A comparison of measured ion temperatures to the 1-D LILAC predictions, showing that measured values are consistently higher than predictions. The error bars display experimental uncertainty (± 0.5 keV).



E10816

Figure 86.23
The ratio of the experimentally measured value of Y_{KOd}/Y_n to the 1-D prediction for different measured Cr. About ~60% is obtained for the shots using 0.35-THz, 2-D SSD, and ~80% is obtained for the shots using 1-THz, 2-D SSD + PS. This ratio approaches unity, while YOC is considerably smaller ($\leq 30\%$). The error bars indicate experimental uncertainties (~10% for neutrons, ~20% for charged particles).



E10815

Figure 86.22
(a) The ratio of measured primary neutron yield to clean 1-D prediction (YOC) plotted against the measured convergence ratio. An average of ~18% is obtained for the shots using 0.35-THz, 2-D SSD, while an average of ~30% is obtained for the shots using 1-THz, 2-D SSD + PS. (b) The ratio of measured KO deuteron yield to 1-D prediction (Y_{KOd}/Y_{1-D}) has an average of ~10% for the shots using 0.35-THz, 2-D SSD and of ~24% for the shots using 1-THz, 2-D SSD + PS. The error bars indicate experimental uncertainties (~10% for neutrons, ~20% for charged particles).

2. Shell Performance of Moderate-Convergence Capsule Implosions

The shell performance discussed in this section is based on measurements of ρR_{shell} and shell electron temperature T_e . The ρR_{shell} can be determined directly from the yield of knock-on protons (this is a temperature-independent method). Once ρR_{shell} is known and ρR_{fuel} has been determined as described in the previous section, the shell T_e can be estimated from the energy downshift of the deuteron and/or triton spectrum (slowing down of these particles is sensitive to T_e). Alternatively, if the shell T_e is already known from other measurements, then the deuteron and/or triton downshifts can be used in an independent estimation of ρR_{shell} .

Knock-on protons are generated only in the CH shell, and typical proton spectra are shown in Figs. 86.15(c) and 86.16(c). Values of ρR_{shell} can be calculated from the proton yields with Fig. 86.14. As displayed in Fig. 86.24, an average ρR_{shell} of ~45 mg/cm² is obtained for shots using 0.35-THz, 2-D SSD without PS, while an average ρR_{shell} of ~60 mg/cm² is obtained for 1-THz, 2-D SSD + PS. A 35% increase of the ρR_{shell} is thus obtained due to the improvement of single-beam uniformity. Figure 86.25 displays a 1-D calculated knock-on proton spectrum overlaid on an experimentally measured proton spectrum for shot 20698. The agreement between these two spectra suggests that, with full beam smoothing, shell performance of a moderate-convergence implosion is close to the 1-D prediction.

The directly determined value of ρR_{fuel} (described in the previous section), together with the measured energy loss of the deuteron and/or triton knock-ons, can also be used to determine shell T_e (if ρR_{shell} has been determined as described in the previous paragraph) or to study ρR_{shell} (if the shell T_e is known). As deuteron and/or triton knock-ons from the fuel travel through fuel and shell, they lose an amount of energy directly proportional to the areal density of the materials they pass through (assuming there is no particle acceleration, as discussed below in Subsection 4). Because these particles are not so energetic, their stopping power is not characterized as “cold plasma stopping,” where there is no temperature dependence, but “warm plasma stopping,” where there is a temperature dependence. The energy loss can be calculated from the stopping power in a fully ionized plasma:^{31,32}

$$\frac{dE}{dx} = - \left(\frac{Z^2 \omega_p e}{v_t} \right)^2 \times \left[G(x^{t/f}) \ell n \Lambda + \theta(x^{t/f}) \ell n \left(1.123 \sqrt{x^{t/f}} \right) \right], \quad (7)$$

where $\theta(x^{t/f})$ is a step function and equals 0 (1) when $x^{t/f} < 1$ (> 1); $\omega_p = (4\pi n_e e^2 / m_e)^{1/2}$ is the electron plasma frequency; Z is the charge of the incident charged particle; v_t (v_f) is the velocity of a test (field) charged particle; $x^{t/f} = v_t^2 / v_f^2$; and $\ell n \Lambda$ is the Coulomb logarithm. $G(x^{t/f})$ is defined as

$$G(x^{t/f}) = \mu(x^{t/f}) - \frac{m_f}{m_t} \left\{ \frac{d\mu(x^{t/f})}{dx^{t/f}} - \frac{1}{\ell n \Lambda} \left[\mu(x^{t/f}) + \frac{d\mu(x^{t/f})}{dx^{t/f}} \right] \right\}, \quad (8)$$

where

$$\mu(x^{t/f}) = 2 \int_0^{x^{t/f}} e^{-\xi} \sqrt{\xi} d\xi / \sqrt{\pi}$$

is the Maxwell integral and m_t (m_f) is the mass of the test (field) particle. Since the effects of large-angle scattering are negligible for charged particles traveling in plasmas of interest,³² the areal density through which a charged particle travels with an energy loss ($\Delta E \approx E_0 - E$) can be approximately determined as

$$\rho R = \int_E^{E_0} \rho \left(\frac{dE}{dx} \right)^{-1} dx. \quad (9)$$

Because of the relatively high temperature and low density of the fuel plasma, the energy loss is dominated by the lower-temperature but higher-density shell plasma. The total areal density is defined as $\rho R_{\text{total}} = \rho R_{\text{fuel}} + \rho R_{\text{shell}}$.

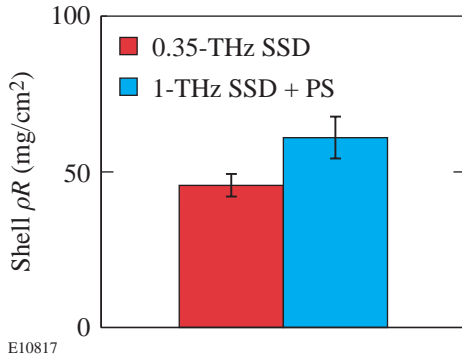


Figure 86.24
An average measured ρR_{shell} of ~ 45 mg/cm² is obtained for the shots using 0.35-THz, 2-D SSD, and a ρR_{shell} of ~ 60 mg/cm² is obtained for the shots using 1-THz, 2-D SSD + PS. The error bars display statistical uncertainties.

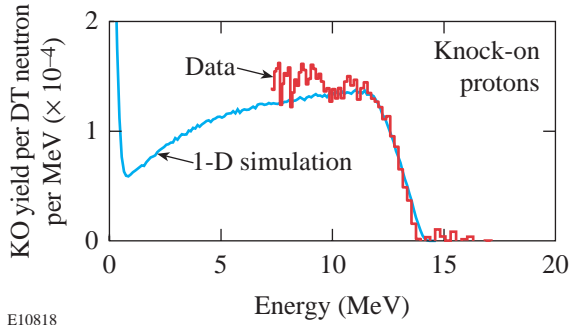


Figure 86.25
A comparison of the measured knock-on proton spectrum (red line) to the 1-D LILAC prediction (blue line) for shot 20698. The agreement between these two spectra suggests the compressed shell has nearly 1-D performance. (The fact that the predicted spectrum is not flat, and decays in the region between 0 to 8 MeV, is due to the fact that low-energy protons generated during the stagnation phase of the implosion may experience a large ρR_{shell} and be ranged out.)

The downshifts of the spectra shown in Figs. 86.16(a) and 86.16(b) (for shot 20698) are about 5 MeV for tritons and 4 MeV for deuterons. To be consistent with the temperature-independent, knock-on-derived values of $\rho R_{\text{fuel}} \sim 14 \text{ mg/cm}^2$ and $\rho R_{\text{shell}} \sim 64 \text{ mg/cm}^2$ calculated as described above for this shot, the value of shell T_e must be about 0.6 keV. A summary of calculated shell T_e values for different shots is given in Fig. 86.26. Shell T_e appears insensitive to single-beam irradiation uniformity, to first order, although some subtle issues such as time and spatial dependence of the knock-on spectra are involved in this determination. This topic is a subject for future study.

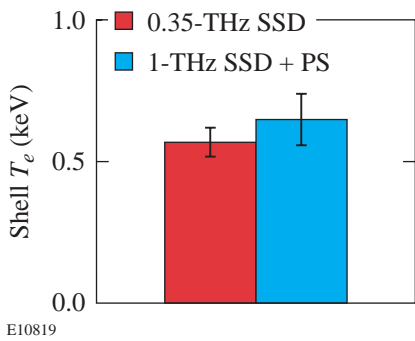


Figure 86.26 Average electron temperatures inferred from the knock-on spectra. Values of ~0.58 keV and ~0.65 keV are obtained for the shots using 0.35-THz, 2-D SSD and 1 THz, 2-D SSD + PS, respectively. The error bars display statistical uncertainties.

3. Similarity to D₂-Filled-Capsule Implosions

With similar experimental conditions, implosions of DT- and D₂-gas-filled plastic capsules are “hydrodynamically” equivalent. While some subtle differences, such as the mass, fusion cross section, equation of the state, etc., still exist, the basic capsule performance is expected to be similar. Recent work¹¹ has resulted in the study of fuel and shell parameters for D₂ shots on OMEGA by measuring spectra of secondary D³He protons. Those numbers are very similar to the knock-on-inferred numbers for related DT shots, as shown in Table 86.I. In general, the inferred and estimated ρR_{fuel} and ρR_{shell} along with ρR_{total} are very similar for both DT- and D₂-capsule implosions under similar experimental conditions. While the corresponding values of YOC are similar, DT implosions result in higher ion temperatures than D₂ implosions. The improvement of the single-beam irradiation uniformity enhances the target performance of both DT and D₂ implosions: ρR_{fuel} (ρR_{shell}) increases ~60% (~35%) for DT implosions and ~65% (~40%) for D₂ implosions; Y_n increases ~80% for both DT and D₂ implosions; YOC increases ~60% for DT and ~80% for D₂ implosions. Ion temperatures are not so sensitive to the uniformity improvement ($\leq 10\%$).

4. Capsule Charging and Particle Acceleration

Time-dependent capsule charging is an essential issue in a spherical implosion. This charging may result in a strong electric field surrounding the capsule and an acceleration of emitted charged particles. Since the measurement of areal densities of imploded capsules through charged-particle spectroscopy relies on accurate determination of particle-energy downshift due to slowing in the capsule, any particle acceleration could introduce serious errors.

Table 86.I: Comparison of DT- and D₂-gas-filled-plastic-shell implosions (the D₂ numbers are from Ref. 11).

Capsules	Single-beam smoothing	T_i (keV)	Y_n	YOC	Y_{Kod}/Y_{1-D}	Y_{2p}/Y_{1-D}	ρR_{fuel} (mg/cm ²)	ρR_{shell} (mg/cm ²)	ρR_{total} (mg/cm ²)
DT (15) CH(20)	0.3-THz, 2-D SSD	4.1±0.5	(6.2±1.4)×10 ¹²	0.18	0.10	—	9.3±1.9	46.8±7.6	~56*
	1-THz, 2-D SSD + PS	4.4±0.5	(1.1±0.3)×10 ¹³	0.30	0.24	—	15.3±2.1	61.4±6.9	~76*
D ₂ (15) CH(20)	0.3-THz, 2-D SSD	3.4±0.5	(8.8±0.8)×10 ¹⁰	0.18	—	0.13	10.0±2.0	~43**	52
	1-THz, 2-D SSD + PS	3.7±0.5	(1.6±0.5)×10 ¹⁰	0.33	—	0.21	14.0±7.4	~57**	72
*Estimated based on measured ρR_{fuel} and ρR_{shell} .									
**Estimated based on measured ρR_{fuel} and ρR_{total} .									

Many previous experiments have demonstrated the existence of capsule charging and particle acceleration, even (unexpectedly) on OMEGA with laser intensities of $\sim 10^{15}$ W/cm² and 351-nm wavelength (where energy upshifts of ~ 1 MeV have been observed for charged-fusion products and ablator protons^{10,33,34}). The hot electrons generated by laser-plasma instabilities in the corona are thought to cause this capsule charging. Earlier experiments also suggest that the charge is time dependent.

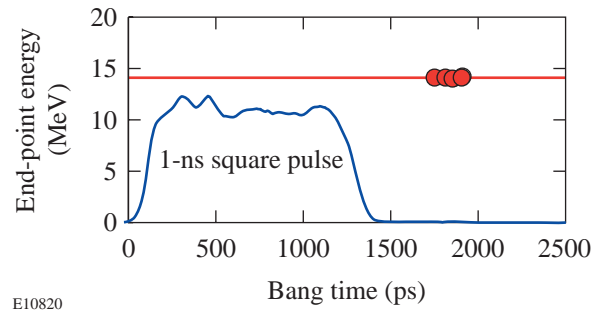
For estimating the effects of the electric fields on charged-fusion products, it has previously been assumed that such effects are important only when the bang time occurs while the laser is on (for example, for a thin-glass-shell capsule driven by 1-ns square pulse).^{35,36} Such effects are assumed unimportant when the bang time occurs several hundreds of picoseconds after the laser turns off, when the electric field has largely decayed away (for example, a thick-plastic-shell capsule driven by a 1-ns square pulse^{10,33}). For the latter case, possible energy upshifts, if any, have been assumed to be completely negligible. Although widely used when determining the spectral downshifts of charged particles,^{10,33} these assumptions have never been directly proven by experiments because the effects of particle acceleration and slowing down are always mixed in an implosion for charged-fusion products.

The knock-on proton data described in this article provide direct proof of this assumption for thick-plastic-shell capsules driven by 1-ns square laser pulses. Any acceleration would cause the upper end points of the knock-on proton spectra to be up-shifted relative to the 14-MeV end point of the birth spectrum. In Figs. 86.15(c) and 86.16(c), the end points of the knock-on proton spectra are precisely (within statistical errors) at 14 MeV, which indicates that the protons are subject to no accelerations. Figure 86.27 shows the measured end points of these and other knock-on proton spectra for a number of shots, plotted against the bang time (a typical 1-ns square pulse on OMEGA is also displayed for reference). The laser pulse has completely ended at ~ 1400 ps, while the bang time occurs several hundreds of picoseconds later. No energy upshifts are observed.

5. Relevance to OMEGA Cryogenic-Capsule Implosions

Plans exist to implode on OMEGA cryogenic DT capsules that typically have low-pressure DT-gas fill in the center surrounded by about 90 μm of DT ice with $\sim 2 \mu\text{m}$ of CH as an ablator. These implosions are predicted to generate DT primary yields $>10^{13}$, with an ion temperature between 1 to 4 keV and areal densities up to ~ 300 mg/cm². Nuclear diagnos-

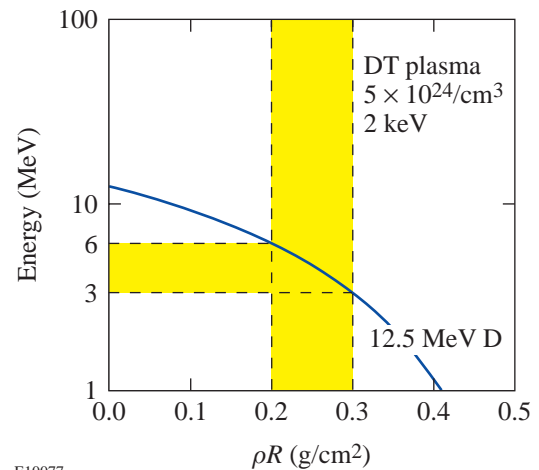
tics will play an important role in the OMEGA cryogenic program. Figure 86.28 shows the energy of knock-on deuterons plotted against their range (ρR) in a DT plasma (an electron temperature of 2 keV and an ion density of 5×10^{24} are assumed, although the density effects on these calculations are weak^{31,32}). For a typical areal density of 200 to 300 mg/cm², a knock-on deuteron will lose about 6 to 9 MeV as it traverses the capsule, and the remaining energy of 3 to 6 MeV is readily detectable using CPS.¹²



E10820

Figure 86.27

The measured upper-energy end points of the knock-on proton spectra for a number of shots in this study are plotted against the bang time (a typical 1-ns square pulse with an arbitrary unit for laser intensity on OMEGA is also displayed for reference). As seen, the laser pulse has completely ended at ~ 1400 ps, while the bang times occur at 1750 to 1950 ps. The energies match the maximum scattered-proton energy, indicating that there are no energy upshifts.



E10077

Figure 86.28

The energy of knock-on deuterons versus their range (ρR) in a DT plasma. In this calculation, an electron temperature of 2 keV and an ion density of 5×10^{24} have been assumed. For a typical predicted areal density of 200 to 300 mg/cm² for a cryogenic-capsule implosion, a knock-on deuteron will lose about 6 to 9 MeV of energy, and the residual energy (3 to 6 MeV) left after leaving the target is readily detectable using charged-particle spectrometry.

Summary and Conclusions

Direct-drive implosions of DT-gas-filled plastic capsules were studied using nuclear diagnostics on OMEGA. In addition to the traditional neutron measurements, comprehensive and high-resolution spectra of knock-on deuterons, tritons, and protons were obtained for the first time in ICF experiments and used to characterize target performance.

Target performance is improved, for moderate-convergence implosions ($Cr \sim 10$ to 20), with the reduction of on-target irradiation nonuniformity that results from an improvement in beam-to-beam laser energy balance and an enhancement of single-beam uniformity. With the use of a 1-THz bandwidth of smoothing by spectral dispersion and polarization smoothing, $Y_n \sim 1.1 \times 10^{13}$, $YOC \sim 0.3$, $\rho R_{\text{fuel}} \sim 15 \text{ mg/cm}^2$, and $\rho R_{\text{shell}} \sim 60 \text{ mg/cm}^2$, which are, respectively, approximately 80%, 60%, 60%, and 35% higher than those determined when using a 0.35-THz bandwidth of smoothing by spectral dispersion. Polarization smoothing of individual laser beams is believed to play an important role.

With full beam smoothing, these implosions have some performance parameters close to one-dimensional-code predictions (e.g., a measured ratio of Y_{KOd}/Y_n achieves $\sim 80\%$ of 1-D predictions). Data suggest that high irradiation uniformity results in reduced Rayleigh–Taylor growth and improved shell integrity. In addition, a brief comparison demonstrates the hydrodynamic “equivalence” of DT-filled capsules and D_2 -filled capsules for moderate-convergence implosions.

ACKNOWLEDGMENT

We express our appreciation to the OMEGA Laser and Experimental Operations and Target Fabrication crews for their excellent work and continuous support. This work has been supported in part by LLE (subcontract P0410025G) and LLNL (subcontract B313975), and by the U.S. Department of Energy Office of Inertial Confinement Fusion under Cooperative Agreement NO. DE-FC03-92SF19460, the University of Rochester, and New York State Energy Research and Development Authority. The support of DOE does not constitute an endorsement by DOE of the views expressed in this work.

REFERENCES

1. J. D. Lindl, R. L. McCrory, and E. M. Campbell, *Phys. Today* **45**, 32 (1992).
2. J. D. Lindl, *Inertial Confinement Fusion: The Quest for Ignition and Energy Gain Using Indirect Drive* (Springer-Verlag, New York, 1998).
3. S. W. Haan *et al.*, *Phys. Plasmas* **2**, 2480 (1995).
4. T. R. Boehly, D. L. Brown, R. S. Craxton, R. L. Keck, J. P. Knauer, J. H. Kelly, T. J. Kessler, S. A. Kumpan, S. J. Loucks, S. A. Letzring, F. J. Marshall, R. L. McCrory, S. F. B. Morse, W. Seka, J. M. Soures, and C. P. Verdon, *Opt. Commun.* **133**, 495 (1997).
5. R. L. McCrory, R. E. Bahr, R. Betti, T. R. Boehly, T. J. B. Collins, R. S. Craxton, J. A. Delettrez, W. R. Donaldson, R. Epstein, J. Frenje, V. Yu. Glebov, V. N. Goncharov, O. V. Gotchev, R. Q. Gram, D. R. Harding, D. G. Hicks, P. A. Jaanimagi, R. L. Keck, J. Kelly, J. P. Knauer, C. K. Li, S. J. Loucks, L. D. Lund, F. J. Marshall, P. W. McKenty, D. D. Meyerhofer, S. F. B. Morse, R. D. Petrasso, P. B. Radha, S. P. Regan, S. Roberts, F. Séguin, W. Seka, S. Skupsky, V. A. Smalyuk, C. Sorce, J. M. Soures, C. Stoeckl, R. P. J. Town, M. D. Wittman, B. Yaakobi, and J. D. Zuegel, “OMEGA ICF Experiments and Preparation for Direct-Drive Ignition on NIF,” to be published in the *Proceedings of the 18th IAEA Fusion Energy Conference*.
6. J. M. Soures, R. L. McCrory, C. P. Verdon, A. Babushkin, R. E. Bahr, T. R. Boehly, R. Boni, D. K. Bradley, D. L. Brown, R. S. Craxton, J. A. Delettrez, W. R. Donaldson, R. Epstein, P. A. Jaanimagi, S. D. Jacobs, K. Kearney, R. L. Keck, J. H. Kelly, T. J. Kessler, R. L. Kremens, J. P. Knauer, S. A. Kumpan, S. A. Letzring, D. J. Lonobile, S. J. Loucks, L. D. Lund, F. J. Marshall, P. W. McKenty, D. D. Meyerhofer, S. F. B. Morse, A. Okishev, S. Papernov, G. Pien, W. Seka, R. Short, M. J. Shoup III, M. Skeldon, S. Skupsky, A. W. Schmid, D. J. Smith, S. Swales, M. Wittman, and B. Yaakobi, *Phys. Plasmas* **3**, 2108 (1996).
7. D. D. Meyerhofer, J. A. Delettrez, R. Epstein, V. Yu. Glebov, V. N. Goncharov, R. L. Keck, R. L. McCrory, P. W. McKenty, F. J. Marshall, P. B. Radha, S. P. Regan, S. Roberts, W. Seka, S. Skupsky, V. A. Smalyuk, C. Sorce, C. Stoeckl, J. M. Soures, R. P. J. Town, B. Yaakobi, J. D. Zuegel, J. Frenje, C. K. Li, R. D. Petrasso, D. G. Hicks, F. H. Séguin, K. Fletcher, S. Padalino, M. R. Freeman, N. Izumi, R. Lerche, T. W. Phillips, and T. C. Sangster, *Phys. Plasmas* **8**, 2251 (2001).
8. F. J. Marshall, J. A. Delettrez, V. Yu. Glebov, R. P. J. Town, B. Yaakobi, R. L. Kremens, and M. Cable, *Phys. Plasmas* **7**, 1006 (2000).
9. F. J. Marshall, J. A. Delettrez, R. Epstein, V. Yu. Glebov, D. R. Harding, P. W. McKenty, D. D. Meyerhofer, P. B. Radha, W. Seka, S. Skupsky, V. A. Smalyuk, J. M. Soures, C. Stoeckl, R. P. Town, B. Yaakobi, C. K. Li, F. H. Séguin, D. G. Hicks, and R. D. Petrasso, *Phys. Plasmas* **7**, 2108 (2000).
10. C. K. Li, D. G. Hicks, F. H. Séguin, J. A. Frenje, R. D. Petrasso, J. M. Soures, P. B. Radha, V. Yu. Glebov, C. Stoeckl, D. R. Harding, J. P. Knauer, R. L. Kremens, F. J. Marshall, D. D. Meyerhofer, S. Skupsky, S. Roberts, C. Sorce, T. C. Sangster, T. W. Phillips, M. D. Cable, and R. J. Leeper, *Phys. Plasmas* **7**, 2578 (2000).
11. F. H. Séguin, C. K. Li, D. G. Hicks, J. A. Frenje, K. M. Green, R. D. Petrasso, J. M. Soures, D. D. Meyerhofer, V. Yu. Glebov, C. Stoeckl, P. B. Radha, S. Roberts, C. Sorce, T. C. Sangster, M. D. Cable, S. Padalino, and K. Fletcher, “Using Secondary Proton Spectra to Study Imploded D_2 -Filled Capsules at the OMEGA Laser Facility,” submitted to *Physics of Plasmas*.

12. J. A. Frenje, K. M. Green, C. K. Li, F. H. Séguin, R. D. Petrasso, S. Roberts, V. Yu. Glebov, D. D. Meyerhofer, J. M. Soures, D. G. Hicks, T. W. Phillips, T. C. Sangster, K. Fletcher, L. Baumgart, H. Olliver, S. Padalino, S. Thompson, and B. White, "Diagnostic Measurements of Charged Particles from DD, D³He, and DT Implosions at the OMEGA Laser Facility Using CR-39 Particle Detectors," to be submitted to Review of Scientific Instruments.
13. P. B. Radha, S. Skupsky, R. D. Petrasso, and J. M. Soures, *Phys. Plasmas* **7**, 1531 (2000).
14. S. Skupsky and R. S. Craxton, *Phys. Plasmas* **6**, 2157 (1999).
15. V. Yu. Glebov, D. D. Meyerhofer, and C. Stoeckl, *Bull. Am. Phys. Soc.* **45**, 144 (2000).
16. M. A. Russotto and R. L. Kremens, *Rev. Sci. Instrum.* **61**, 3125 (1990).
17. J. D. Kilkenny, M. D. Cable, C. A. Clower, B. A. Hammer, V. P. Karpenko, R. L. Kauffman, H. N. Kornblum, B. J. MacGowan, W. Olson, T. J. Orzechowski, D. W. Phillion, G. L. Tietbohl, J. E. Trebes, B. Chrien, B. Failor, A. Hauer, R. Hockaday, J. Oertel, R. Watt, C. Ruiz, G. Cooper, D. Hebron, L. Leeper, J. Porter, and J. Knauer, *Rev. Sci. Instrum.* **66**, 288 (1995).
18. R. J. Leeper, G. A. Chandler, G. W. Cooper, M. S. Derzon, D. L. Fehl, D. L. Hebron, A. R. Moats, D. D. Noack, J. L. Porter, L. E. Ruggles, J. A. Torres, M. D. Cable, P. M. Bell, C. A. Clower, B. A. Hammel, D. H. Kalantar, V. P. Karpenko, R. L. Kauffman, J. D. Kilkenny, F. D. Lee, R. A. Lerche, B. J. MacGowan, M. J. Moran, M. B. Nelson, W. Olson, T. J. Orzechowski, T. W. Phillips, D. Ress, G. L. Tietbohl, J. E. Trebes, R. J. Bartlett, R. Berggren, S. E. Caldwell, R. E. Chrien, B. H. Failor, J. C. Fernandez, A. Hauer, G. Idzorek, R. G. Hockaday, T. J. Murphy, J. Oertel, R. Watt, M. Wilke, D. K. Bradley, J. Knauer, R. D. Petrasso, and C. K. Li, *Rev. Sci. Instrum.* **68**, 868 (1997).
19. R. A. Lerche, D. W. Phillion, and G. L. Tietbohl, *Rev. Sci. Instrum.* **66**, 933 (1995).
20. D. G. Hicks, C. K. Li, R. D. Petrasso, F. H. Séguin, B. E. Burke, J. P. Knauer, S. Cremer, R. L. Kremens, M. D. Cable, and T. W. Phillips, *Rev. Sci. Instrum.* **68**, 589 (1997).
21. D. G. Hicks, "Charged Particle Spectroscopy: A New Window on Inertial Confinement Fusion," Ph.D. thesis, Massachusetts Institute of Technology, 1999.
22. F. H. Séguin *et al.*, "A Proton Spectrometer Based on a Wedge-Shaped Range Filter and CR39 Nuclear Track Detectors," to be submitted to Review of Scientific Instruments.
23. S. Skupsky and S. Kacenjar, *J. Appl. Phys.* **52**, 2608 (1981).
24. S. Kacenjar, S. Skupsky, A. Entenberg, L. Goldman, and M. Richardson, *Phys. Rev. Lett.* **49**, 463 (1982).
25. E. M. Campbell *et al.*, *J. Appl. Phys.* **51**, 6062 (1980).
26. M. D. Cable and S. P. Hatchett, *J. Appl. Phys.* **62**, 2233 (1987).
27. H. Azechi, M. D. Cable, and R. O. Stapf, *Laser Part. Beams* **9**, 119 (1991).
28. R. D. Petrasso, C. K. Li, M. D. Cable, S. M. Pollaine, S. W. Haan, T. P. Bernat, J. D. Kilkenny, S. Cremer, J. P. Knauer, C. P. Verdon, and R. L. Kremens, *Phys. Rev. Lett.* **77**, 2718 (1996).
29. S. Cremer, C. P. Verdon, and R. D. Petrasso, *Phys. Plasmas* **5**, 4009 (1998).
30. E. Goldman, Laboratory for Laser Energetics Report No. 16, University of Rochester (1973).
31. C. K. Li and R. D. Petrasso, *Phys. Rev. Lett.* **70**, 3059 (1993).
32. C. K. Li and R. D. Petrasso, *Phys. Plasmas* **2**, 2460 (1995).
33. D. G. Hicks, C. K. Li, F. H. Séguin, A. K. Ram, J. A. Frenje, R. D. Petrasso, J. M. Soures, V. Yu. Glebov, D. D. Meyerhofer, S. Roberts, C. Sorce, C. Stockl, T. C. Sangster, and T. W. Phillips, *Phys. Plasmas* **7**, 5106 (2000).
34. D. G. Hicks, C. K. Li, F. H. Séguin, J. D. Schnittman, A. K. Ram, J. A. Frenje, R. D. Petrasso, J. M. Soures, D. D. Meyerhofer, S. Roberts, C. Sorce, C. Stoeckl, T. C. Sangster, and T. W. Phillips, *Phys. Plasmas* **8**, 606 (2001).
35. Y. Gazit, J. Delettrez, T. C. Bristow, A. Entenberg, and J. Soures, *Phys. Rev. Lett.* **43**, 1943 (1979).
36. J. Delettrez, A. Entenberg, Y. Gazit, D. Shvarts, J. Virmont, T. Bristow, J. M. Soures, and A. Bennish, *Nucl. Fusion* **23**, 1135 (1983).